

AperTO - Archivio Istituzionale Open Access dell'Università di Torino

**Dose Attenuation in Innovative Shielding Materials for Radiation Protection in Space:
Measurements and Simulations**

This is a pre print version of the following article:

Original Citation:

Availability:

This version is available <http://hdl.handle.net/2318/1886988> since 2023-01-24T14:49:49Z

Published version:

DOI:10.1667/RADE-22-00147.1

Terms of use:

Open Access

Anyone can freely access the full text of works made available as "Open Access". Works made available under a Creative Commons license can be used according to the terms and conditions of said license. Use of all other works requires consent of the right holder (author or publisher) if not exempted from copyright protection by the applicable law.

(Article begins on next page)

Dose attenuation in innovative shielding materials for radiation protection in space: measurements and simulations

Francesca Luoni ^{1,2}, Daria Boscolo ¹, Gianluca Fiore ³, Luca Bocchini ⁴, Felix Horst ¹, Claire-Anne Reidel ¹, Christoph Schuy ¹, Claudio Cipriani ⁴, Andrea Binello ³, Marcello Baricco ³, Martina Giraudo ⁴, Giovanni Santin ^{5,6}, Marco Durante ^{1,2}, Uli Weber ¹

¹Biophysics Department, GSI Helmholtzzentrum für Schwerionenforschung GmbH, Planckstr. 1 64291

Darmstadt, Germany

²Institut für Physik Kondensierter Materie, Technische Universität Darmstadt, Karolinenpl. 5 64283

Darmstadt, Germany

³Chemistry Department, Università di Torino, Via Pietro Giuria 7 10125 Torino, Italy

⁴Thales Alenia Space Italia, Strada Antica di Collegno 253 10146 Torino, Italy

⁵RHEA System, Jonckerweg 18 2201 DZ Noordwijk, Netherlands

⁶ESA ESTEC, Keplerlaan 1 2201 AZ Noordwijk, Netherlands

Corresponding author: Uli Weber, u.weber@gsi.de

Abstract

Galactic cosmic rays (GCR) are the number one hindrance to manned space exploration. Currently, the most realistic way to reduce the dangers caused by GCR to acceptable levels is passive shielding. Light materials guarantee the strongest dose attenuation per unit mass. High-density polyethylene is considered the gold standard for radiation protection in space. Nevertheless, accelerator-based experimental campaigns already showed the advantages of more hydrogen-rich innovative shielding materials such as lithium hydride. The experimental campaigns of this work focused on the absorbed dose attenuation properties of lithium-based hydrides chemically stabilised with a paraffin matrix. Such materials were compared to pure lithium-based hydrides, polyethylene, structural materials such as spacecraft aluminium alloys and lithium batteries, and *in situ* shielding materials such as Moon regolith and its main components silicon and silicon dioxide. The experimental results were compared to simulations performed with PHITS, FLUKA, and Geant4, which are among the most commonly used Monte Carlo codes for radiation protection in space. The simulations showed systematic differences and highlighted the pressing need for reliable nuclear cross-section models.

Keywords:

Shielding in space, absorbed dose measurements, lithium-based hydrides, Moon regolith, Monte Carlo simulations

1 Introduction

The dangers due to galactic cosmic rays (GCR) (Simpson, 1983) are the biggest hindrance to manned long-term deep-space exploration missions (Durante & Cucinotta, 2011; Cucinotta et al., 2013; Chancellor et al., 2014; Kennedy, 2014). Currently, the most promising radiation protection strategy is passive shielding (Council et al., 2008; Durante & Cucinotta, 2011; Washburn et al., 2015). However, the severe mass constraints of long-term space missions combined with the high penetration power of GCR, make it practically impossible to stop them within the shielding material. Therefore, the most efficient strategy to mitigate the effect of GCR is to exploit nuclear fragmentation processes and break heavy ions into lighter and lower-LET (linear energy transfer) particles, which are less dangerous because of their lower relative biological effectiveness (Zeitlin & La Tessa, 2016). The quantity to be maximised with the choice of shielding materials is the nuclear fragmentation cross-section per unit mass of material. This quantity scales as $A_s^{-1/3}$, A_s being the mass number of the shield. Therefore, light materials are considered to be the best option for passive shielding purposes (Miller et al., 2003; Shavers et al., 2004; Zeitlin et al., 2006; Guetersloh et al., 2006; Durante & Cucinotta, 2011).

The ROSSINI3 project aimed at testing stable and manageable high-performance shielding materials. The project was funded by the European Space Agency and is a collaboration of Thales Alenia Space Italia, GSI Helmholtzzentrum für Schwerionenforschung, and the University of Torino.

The main GCR contributors to dose equivalent behind thin shields are iron ions (Durante & Cucinotta, 2011) and their energy spectrum peaks around 1 GeV/u. Therefore, several accelerator-based experimental campaigns making use of high-energy (0.4 to 1 GeV/u) ^{56}Fe beams, were conducted in the past years (La Tessa et al., 2005; Zeitlin et al., 2006, 2008; Lobascio et al., 2008; Castellanos et al., 2017; Boscolo et al., 2020). In the framework of this work, dose attenuation curves for 1 GeV/u ^{56}Fe beams have been measured with the aim of directly comparing the dose-attenuation properties of lithium-based hydrides and their composites to other structural and potential shielding materials.

One could argue that, the comparison of the shielding effectiveness of different materials by using absorbed dose measurements performed with a single-energy and single-ion beam, is not significant *per se*. The galactic (and intergalactic) cosmic ray spectrum composition is in fact, rich both in ions, spanning from H to Ni, and in energies, from a few MeV up to the ZeV region. In addition, the most significant quantity to take care of is the endpoint-dependent relative biological effectiveness of the mixed radiation field composed of primary GCR and the secondary particles produced in the shield (Borak et al., 2014). Nevertheless, it is crucial to perform such “simple” accelerator-based experiments to compare the experimental results to the outcome of Monte Carlo (MC) simulations. Thanks to this comparison, it is in fact possible to understand more about the validity of the basic physics models underlying the MC codes. The improvement of the models leads also to improvements in the risk model calculations, on which radiation protection of astronauts fully relies. In addition, ^{56}Fe is the most relevant ion species of the GCR spectrum in free space (Durante & Cucinotta, 2011). For these reasons, this study and the corresponding MC benchmark provide valuable data. The thicker the shielding becomes, the higher the contribution of light ions to the dose equivalent is (Norbury et al., 2020). Therefore, experimental campaigns with protons and helium ions are ongoing at the GSI Helmholtz center for Heavy Ion research GmbH and the Heidelberg Ion-Beam Therapy Center.

The materials chosen for the ROSSINI3 experimental campaigns are listed and described in Section 2. Innovative shielding materials such as LiH, LiBH₄, and the same two hydrides stabilised with paraffin were tested and compared to the gold-standard for radiation protection in space: polyethylene (Durante & Cucinotta, 2011; Shavers et al., 2004). The results of the ROSSINI2 program (Giraud et al., 2018; Schuy et al., 2018) suggested in fact, that the dose attenuation tests and simulations in the follow-up ROSSINI3 cam-

paigh should focus on lithium-based hydride materials. In particular, LiH showed promising results in dose attenuation of ^{56}Fe beams within the ROSSINI2 experimental campaigns. Such lithium-based materials have also been the focus of attention of other promising simulation campaigns (Naito et al., 2020). Nevertheless, since pure lithium-based hydrides are chemically reacting with moisture and difficult to handle, new composite materials were created in the framework of the ROSSINI3 project and tested alongside pure samples. A certain amount of paraffin was mixed to the hydrides to make them more stable. The longevity of such materials is discussed in Section 3.1. The production and characterisation of the composite materials was carried out by the chemistry department of the University of Torino. Pure paraffin was tested for comparison. Additionally, structural and *in situ* shielding materials were tested as well. Three different aluminium alloys commonly used in space, i.e. Al2024, Al2219 and Al2195 were compared to each other, as well as lithium batteries. Simulant of polar highland Moon regolith itself was tested as potential *in situ* shielding material, alongside Si and SiO_2 , which are the main components (SiO_2 ca. 50%, see Table 1) of Moon regolith. Some multi-layer configurations involving candidate shielding materials, simulant of Moon sand and concrete, and aluminium were also tested.

The results of the experimental campaigns were compared to the predictions of FLUKA (Ferrari et al., 2005; Böhlen et al., 2014; Aricò et al., 2019), PHITS (Iwase et al., 2002), and Geant4 (Agostinelli et al., 2003), which are among the most commonly used MC codes for radiation protection in space applications.

2 Materials and Methods

2.1 Target materials

LiH was produced by the Alfa Aesar company with a purity of 97+% (CAS number: 7580-67-8), LiBH_4 by Acros Organics with a purity of 95% (CAS: 16949-15-8) and paraffin by Sigma-Aldrich (Paraplast[®], CAS: 145686-99-3). Paraffin wax was selected to be mixed with hydrides, due to its high hydrogen content and relatively easy manufacturing processes (see Appendix A). The composite samples were produced using the highest possible hydride content that still guarantees sufficient mechanical and chemical stability of the samples. In particular 50% hydride content in weight was used for LiH-paraffin, and 40% for LiBH_4 -paraffin. All the pure and composite lithium-based hydrides were embedded into vacuum seal plastic bags (areal density of 0.009 g cm^{-2}) to keep them out of contact with air.

Pure paraffin samples were also prepared for comparison. A simple melting-cooling procedure was performed in air, leading to paraffin samples having a similar size of composites. The procedure was repeated and additional material was added to obtain flat and parallel surfaces. Details about the preparation of the pure and composite lithium-based hydride and pure paraffin samples can be found in Appendix A, alongside the characterisation of their purity and homogeneity.

Three aluminium alloys generally used for structural components of space vehicles, were selected and tested in the ROSSINI3 experimental campaigns: aluminium 2024, 2219 and 2195. All the selected samples belong to the AA 2000 series (alloyed with copper), which is the most extensively used alloy family in aerospace structures, due to its good mechanical properties.

Another material that could potentially become part of the spacecraft structure and that was tested within the ROSSINI3 experimental campaigns, is Li-poly batteries (stacked flat cellphone built-in Lithium polymer batteries without housing, relatively homogenous areal density).

High-density polyethylene (HDPE), golden standard for radiation protection in space, was also used in the experimental campaigns for comparison. Two HDPE wedges have been shifted relative to each other to obtain different material thicknesses.

Table 1: Highland Moon regolith mass percentage composition. LOI stays for Low-Order Impurities.

Element	Mass contibution (%)	Element	Mass contibution (%)
SiO ₂	47.89	Al ₂ O ₃	27.06
TiO ₂	0.52	FeO	3.68
MnO	0.06	MgO	2.84
CaO	14.19	Na ₂ O	2.43
K ₂ O	0.25	P ₂ O ₅	0.2
LOI	0.88		

Other materials used in the experimental campaigns are simulant of highland Moon regolith, pure Si and SiO₂. Moon regolith is in fact a potential *in situ* material, and Si and SiO₂ are among its main components. Cylindrical Si and SiO₂ targets are characterised by a purity of 99 and 99.99%, respectively. The Off Planet Research OPRH2N Near-Side Highland Lunar regolith simulant was used for this experimental campaign. Its composition is reported in Table 1, and it consists of sand with grain diameter between 250 and 500 μm . The Moon simulant was irradiated into a PMMA container with a later area of $5 \times 7 \text{ cm}^2$ and a length of 4 cm. The walls of the box are 0.5 mm thick. A 1 mm-thick plexiglas wall was used to confine the Moon sand. Its relative position was changed at each irradiation so that thicker and thicker Moon layers could be placed.

A complete list of the irradiated materials can be found in Table 2. Error bars for the areal densities of the irradiated targets were estimated through error propagation of the measured weight, thickness and area of the targets, and summed up to obtain the error associated to the areal density of the total irradiated thickness.

2.2 Experimental setup

Irradiations of the described materials were performed with 1 GeV/u ⁵⁶Fe beams in GSI Cave A. Depending on the experimental campaign, the beam intensity ranged between 1 and 3×10^7 ions per spill and the beam full-width-half-maximum (FWHM) between 5 and 10 mm. The setup consisted of variable target thicknesses placed in between two large area parallel-plate ionisation chambers (ICs): the closest to the beam exit window is called IC1 and the other IC2. The active detector thickness is $2 \times 10 \text{ mm}$ for the IC2 and $2 \times 5 \text{ mm}$ for the IC1, with an active area of $26 \times 26 \text{ cm}^2$. It was filled with a gas mixture of 80% argon and 20% CO₂. The electrodes are represented with black lines. They are 6.7 mg cm^{-2} thick and made of a nickel coated polyester mesh (43% and 57% mass percentages, respectively). The outer foils are 25 μm thick and made of BoPET (mylar). The ICs were kept in the same position and the different targets were exchanged between subsequent irradiations. IC1 operated as reference monitor for normalisation. Therefore, the results are not affected by unavoidable fluctuations in the beam intensity. The charge readout of the ionisation chambers was realised with high-precision electrometers (model K6517, KEITHLEY), which guaranteed accuracy in the charge measurement to be below 1‰. The large area of the parallel-plate ionisation chambers, laterally integrates almost the complete signal from the beam. Therefore, the sensitivity of the results to beam width and scattering effects is minimised. The same setup has been largely used in the past (Giraud et al., 2018; Schuy et al., 2018; Pfuhl et al., 2018). A schematic of the experimental setup is reported in Figure 1. For the fine steps around the peak of the paraffin Bragg curve, a so-called range shifter (RS) (Simeonov et al., 2017) was used. It is composed of ten PE foils and plates with well-defined areal densities, each roughly doubling in size. Since it is remotely controlled, it allows a quick change of the amount of material in the beamline,

Table 2: List of all single materials used in this study alongside their mass densities (ρ), areas perpendicular to the beamline (A) and irradiated thicknesses (t), with associated uncertainties. The thicknesses are given in areal densities. LiH_p and LiBH_{4 p} stay for LiH and LiBH₄ stabilised with paraffin. The numbers in parentheses refer to the uncertainties of the values, and apply to the least significant digits.

Material	ρ (g cm ⁻³)	A (cm ²)	t (g cm ⁻²) ^a
LiH	0.5279(48)	33.20(51)	0.615(13), 1.231(16), 1.863(19), 2.481(26), 3.096(29), 3.710(31), 4.315(34), 4.937(37), 5.543(39), 6.149(41), 6.756(42), 7.359(44), 7.959(46), 8.559(47)
LiBH ₄	0.5255(59)	33.20(51)	0.633(11), 1.264(18), 1.897(22), 2.525(27), 3.149(32), 3.758(34), 4.383(37), 5.003(39), 5.637(42), 6.261(45)
LiH _p	0.7844(50)	77.73(31)	0.733(13), 1.477(16), 2.227(21), 2.969(23), 3.718(25), 4.456(28), 5.216(30), 5.965(32), 6.731(34), 7.486(35), 8.232(37), 9.018(39), 9.721(40), 10.504(42), 11.267(45)
LiBH _{4,p}	0.7523(38)	28.23(19)	0.692(12), 1.277(17), 1.943(19), 2.627(24), 3.326(26), 4.003(28), 4.673(30), 5.353(31), 6.011(32)
Paraffin	0.9025(56)	93.48(55)	1.845(18), ... 34.06(17) ^b
HDPE	0.9270(93)	^c	3.587(37), 4.811(49), 6.016(61), 6.962(70)
Al2024	2.690(55)	402(1)	2.261(18), 3.392(27)
Al2219	2.835(10)	72.00300(11)	2.026(10), 6.079(29), 8.105(38)
Al2195	2.705(28)	129.59(37)	3.646(31), 6.382(50)
Si	2.404(37)	79(2)	0.962(16), 1.923(30), 2.885(45), 3.846(59), 4.808(74), 5.769(88), 6.73(10)
SiO ₂	2.213(32)	79(2)	0.885(13), 1.770(25), 2.656(38), 3.541(51), 4.426(63), 5.311(76), 6.196(89)
Moon regolith	1.345(91)	35.00(86)	0.243(28), 0.65(14), 1.32(15), 1.99(18), 2.66(22), 4.01(31), 5.62(41)
Li-poly batteries	2.270(43)	^d	0.6883(29), 1.3899(64), 2.091(10), 2.789(14), 4.221(21), 6.545(31), 8.896(41), 11.933(53)

^a The thicknesses of the pure and composite lithium-based hydrides include the thin plastic bags they were embedded in during the irradiations, as well as the thicknesses of the Moon regolith simulant include the plexiglas foil and PMMA walls of the box it was irradiated in.

^b The whole Bragg curve was measured for paraffin in steps of 1.8 g cm⁻². At the Bragg peak, the steps are smaller and realised with the HDPE foils of the range shifter.

^c The HDPE target consists of two wedges shifted relatively to each other. Thus, the area of the target changes according to the overlap of the wedges. The wedges have an area of 246 cm² (minimum area) and an angle of 16°.

^d The area of the Li-ion batteries varies from 39 to 59 cm², depending on the battery.

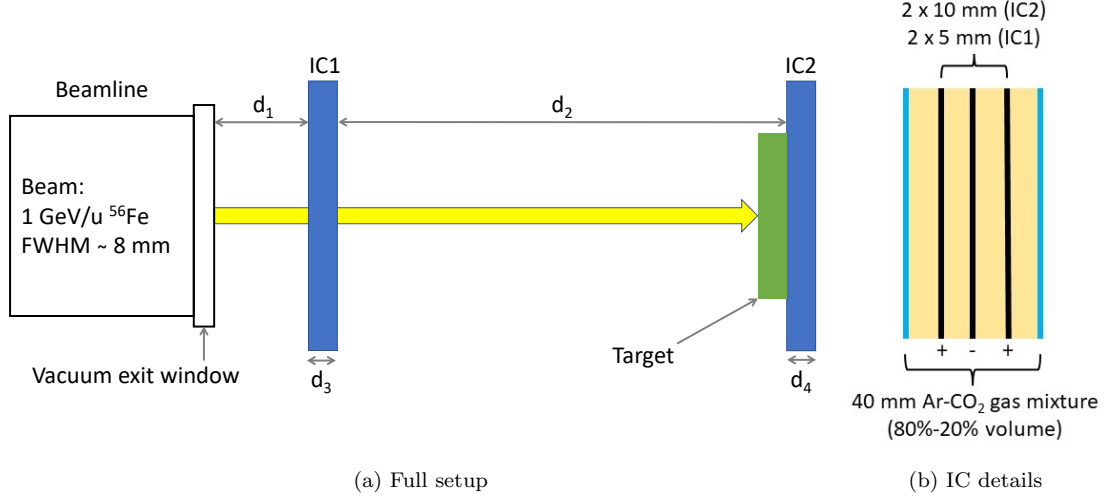


Figure 1: Panel (a): experimental setup. $d_3 = d_4 = 4\text{ cm}$. The distances d_1 and d_2 are beamtime dependent, d_1 being about 15 cm and d_2 about 1 m. The distance between the target and IC2 is also beamtime dependent and varies between 0 and 2 cm. The MC simulations have been performed accordingly. Panel (b): details about the ICs.

174 varying from 62 μm of PE up to 64 mm, in steps of ca. 60 μm . Since PE has almost the
 175 same stoichiometric composition as paraffin, it serves as a good supplement for the paraffin
 176 targets.

177 2.3 Data analysis

178 The ratio of the charge signal from the two ionisation chambers (Q_2/Q_1) normalised to the
 179 same ratio obtained without any target ($Q_{2,\text{no target}}/Q_{1,\text{no target}}$), provides the value for dose
 180 reduction due to the presence of the target:

$$181 \frac{D_2}{D_1} = \frac{Q_2/Q_1}{Q_{2,\text{no target}}/Q_{1,\text{no target}}}. \quad (1)$$

182 For each material thickness (or configuration of materials) at least two measurement points
 183 were taken. The final data were computed as the arithmetic average of these values, and
 184 the associated statistical fluctuations as their standard deviation. The systematic com-
 185 ponent of the errors was evaluated as the standard deviation of the fluctuation (mea-
 186 sured at different times of the experimental campaign) of the data obtained without target
 187 ($Q_{2,\text{no target}}/Q_{1,\text{no target}}$). This accounts for the uncertainty related to the non-linearities of
 188 the readout electronics, e.g. slight offsets.

189 2.4 Monte Carlo simulations

190 Simulations reproducing the ROSSINI3 experimental campaigns were carried out using the
 191 Monte Carlo particle transport codes PHITS (version 3.20), Geant4 (version 10.6 patch-02)
 192 and FLUKA (version 2020.0.3, and flair version 2.3-0 (Vlachoudis et al., 2009)). The main
 193 goal was to keep the simulations as similar as possible to focus on the differences among the
 194 physics models.

195 The simulation geometry reproduced the experimental setup. The dose ratios obtained
 196 for each target thickness simulated, were divided by the dose ratio obtained for the no target

case, as it was done with the experimental data. The doses were calculated in the active regions of the two ICs. The simulations also included the plastic bags and the box into which the lithium-based hydrides and Moon were respectively irradiated. The beam was modeled with a Gaussian lateral profile of 0.8 cm FWHM (no angular divergence), the ICs as two mylar walls filled with gas and no detailed internal electrode structures. Details about the ICs are in fact not crucial, since the dose ratios are normalised to the no target case. For the simulations, the number of generated primary ions has been selected high enough to decrease the statistical errors to less than 3% (10^4 to 10^5 ions).

2.4.1 *Geant4*

In Geant4, the dose in the detector was calculated by summing up the energy deposition in the active region of the detector and dividing it by the mass of the region itself. The default electron range cut of 0.1 mm was used for the pure and composite lithium-based hydrides, and for HDPE. It corresponds to an energy cut of 0.08 MeV in HDPE, and of 0.057 MeV in LiH. A 0.01 mm cut was used for electrons in the aluminium alloys, Si, SiO₂ and Moon regolith. It corresponds to an electron energy of 0.0325 MeV in aluminium, and of 0.03 MeV in Si. The reference physics lists QGSP_INCLXX, FTFP_BERT, and QBBC_EMY Geant4 physics lists were used for the simulations. QGSP_INCLXX is an experimental physics list that uses the Quark Gluon String model for high-energy hadronic interactions, and the Leige Intranuclear Cascade model for proton, neutron and pion induced reaction with low energies, instead of the Binary or Bertini Cascade models. It is recommended to be used for shielding applications (“Geant4 Physics Reference manual, Release 10.6”, 2017). FTFP_BERT makes use of the FRITIOF String model for high-energy hadron interactions, and Bertini for low energies. It is recommended to be used for high-energy applications (“Geant4 Physics Reference manual, Release 10.6”, 2017). QBBC_EMY is a list created *ad hoc* for space, radiation biology, and radiation protection applications. It includes combinations of Binary, Bertini, Quark Gluon String, FRITIOF String and other models to reach high precision in the simulation of many hadron-ion and ion-ion interactions in a wide energy range (Ivantchenko et al., 2012). This last list was chosen for the simulations because of the good agreement with the data presented in (Schuy et al., 2018) and more generally in the energy range between 100 MeV u⁻¹ and 1.5 GeV u⁻¹ (Ivantchenko et al., 2012). Also the reference physics lists QGSP_BERT, QGSP_BERT_EMV, and FTFP_INCLXX, were used to simulate the full paraffin Bragg curve for a deeper study of the differences among the lists themselves and the combination of the different models for different particles and energy ranges.

2.4.2 *PHITS*

In PHITS, the T-Deposit tally was used to calculate the dose deposition. A 1.0×10^{-3} MeV energy cut was used for electrons, gammas, and positrons, while the production threshold for delta rays was set to 0.1 MeV. The transport of electrons, positrons, and photons was based on the EGS5 algorithm, while gamma decay residual nuclei transport was based on the EBITEM model. Landau Vavilov energy straggling option was selected for charged particles and nuclei. The Lynch formula based on the Moliere theory was used for Coulomb diffusion, while JQMD-2.0 and SMM for nuclear reactions.

2.4.3 *FLUKA*

In FLUKA, transport cuts for e^\pm and γ were set to 0.1 MeV, like the delta ray production cut. Projectile and target electromagnetic-dissociation and coalescence processes were activated, and the FLUKA evaporation model used was “New evaporation with heavy frag”.

3 Results and discussion

3.1 Stability of the lithium-based hydrides

As stated above, pure hydrides were mixed with paraffin in homogeneous composite pellets, with the aim of improving the hydrides' stability against moisture. Longevity tests were carried out to confirm the protection of paraffin against the reaction of the hydrides with moisture. The air stability tests are reported in Appendix B. The results show that the addition of the paraffin acts as an effective protective barrier to the hydride phase as the degradation kinetics due to the exposure to air is greatly reduced. Once properly embedded, the composite pellets do not change their chemical composition due to reaction with radiation, i.e. no radiolysis takes place. Such analysis was carried out after irradiation and is presented in greater detail in Appendix C. This can also be seen as a long-time longevity test for the developed materials in practical space applications.

3.2 Dose attenuation results

3.2.1 Experimental data

The measured dose ratio decreases with the increase of the target thickness. This is caused by the attenuation of the primary iron beam due to the fragmentation processes the ^{56}Fe ions undergo while traversing the target material. The produced fragments have a linear energy transfer (LET) lower than ^{56}Fe as $\text{LET} \propto Z_f^2$, where Z_f stands for the atomic number of the fragment. For 1 GeV/u ^{56}Fe ions, the slowing down of the primary beam cannot compensate for the dose reduction due to the fragmentation. Therefore, the dose ratio D_2/D_1 decreases. The analysis of the dose attenuation results has been performed as a function of the areal density of the targets (g cm^{-2}). The more fragmentation per unit mass happens, the stronger dose attenuation is expected for the same areal density of different targets. Lighter materials such as lithium-based hydrides are expected to provide stronger dose attenuation (Durante & Cucinotta, 2011). Heavier materials such as aluminium are expected to be less effective to this purpose.

The dose ratios (see Equation 1) obtained for single materials are plotted in Figure 2. As expected, the dose reduction is stronger for materials with lower mass number. LiH performs the best. The dose reduction obtained with LiBH_4 and the chemically stable LiH_p is the same and the second best after LiH. This result is very interesting as it shows that a chemically stable material can be a better shield from 1 GeV/u ^{56}Fe ions than HDPE, which is the so-far considered gold-standard for radiation protection in space. Aluminium, the main structural material of spacecrafts, is the worst shield among the tested materials. SiO_2 shows a dose reduction stronger than Si because $A_{\text{O}} < A_{\text{Si}}$. The results obtained with Moon regolith and SiO_2 are very similar as SiO_2 is the Moon regolith main component (see Table 1).

In Figure 2, only Al2219 alloy results are reported. A direct comparison between the three aluminium alloys is shown in Figure 3. They show similar dose attenuation curves, but thanks to the high precision of the experimental setup, such small differences can be resolved. However, no big role is expected to be played by the kind of aluminium alloy for radiation protection purposes.

For all the investigated materials, a small dose enhancement can be observed for very small target thicknesses. This phenomenon is called dose build-up (Pfuhl et al., 2018; Carlsson & Carlsson, 1977). More details about it are given in Appendix D.

Dose attenuation measurements were also performed with Li-ion batteries. As it can be seen in Figure 4, they perform better than aluminium in reducing the dose.

Some irradiations were performed merely by exchanging the order of the targets, without changing the material type or quantity. Pure LiH and LiBH_4 were studied for this

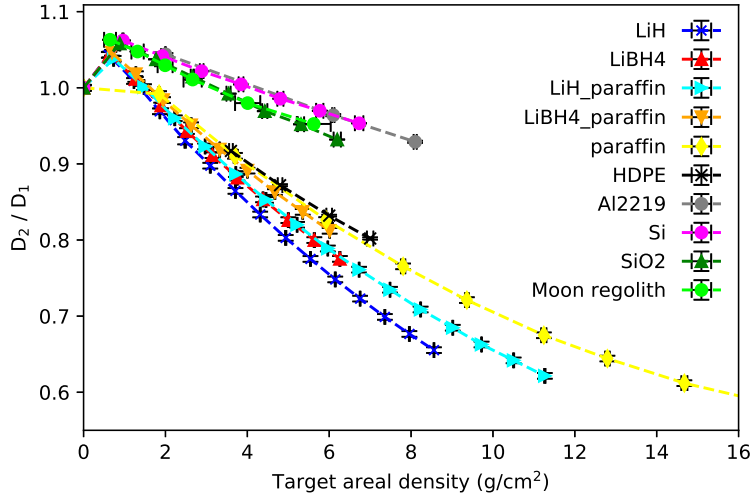


Figure 2: Dose attenuation results for all materials tested. The dashed lines simply connect the experimental points.

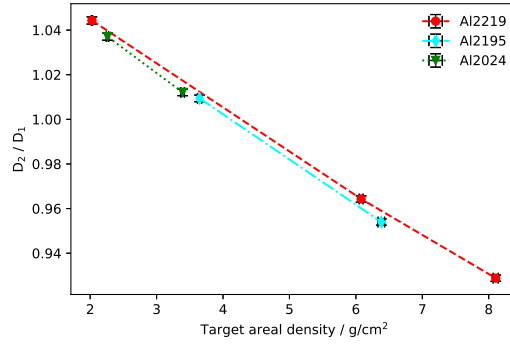


Figure 3: Dose attenuation results obtained with three different aluminium alloys generally used in space. The dashed lines simply connect the experimental points.

purpose, in combination with Al2219 and Al2195 alloys. The results of these exchange experiments are reported in Figure 5, and show that the absorbed dose attenuation is systematically higher (1% effect ca.) if the shielding material (LiH or LiBH₄) is placed upstream of the structural material (aluminium). The reason might be that the combination of energy loss and fragmentation is slightly more beneficial for the configuration in which the shielding material is placed upstream the aluminium. In a real case configuration, this would mean placing the shielding material inside the structural walls of the spacecraft. The consistency of such results is proved by the fact that the dose attenuation for shielding materials placed upstream Al is stronger independently of the choice of the Al alloy, the lithium-based hydride, and their thicknesses. It was already known that the order of the layers can have an impact on the shielding performance (Durante, 2008; Horst et al., 2022). Similar experiments were already performed by (Durante, 2008) with HDPE and aluminium, but did not show such systematic results. The reason is probably that the smaller area of the egg chamber used for those measurements cannot guarantee the same experimental precision of the data presented in this work. It is very interesting to notice that when looking at

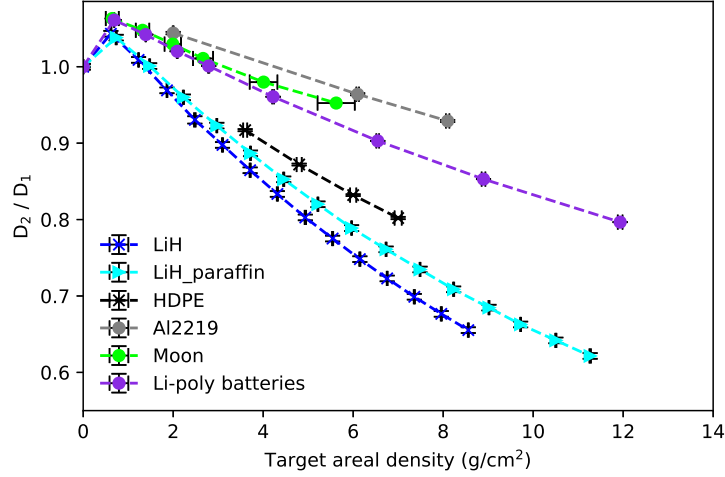


Figure 4: Dose attenuation results obtained with lithium batteries compared to aluminium, Moon regolith, PE, LiH_p and LiH .

dose equivalent the situation gets reversed, as placing the structural material (higher Z) outside and the shielding (lower Z) inside gives better dose equivalent attenuation. Such results have been obtained by (Horst et al., 2022) with MC simulations for very thick shields taking into account also secondary neutrons. It was in fact proven that a stronger dose equivalent reduction is obtained by placing the hydron-rich material inside because of the better moderation of build-up neutrons. This highlights the need for studies involving the biological effectiveness of the shields.

Some realistic multi-layer configurations of spacecraft and *in situ* materials were also used for dose attenuation measurements. The results are presented in Appendix E.

3.2.2 Monte Carlo simulations

Monte Carlo predictions of the experimental results are reported in Figure 6 for the aluminium alloys and HDPE, Figure 7 for the lithium-based hydrides and their composites, and Figure 8 for pure Si, SiO_2 , and Moon regolith. Error bars represent the statistical error due to the use of Monte Carlo approaches. PHITS reproduces well the results for aluminium and all the pure and composite lithium-based hydrides. On the other hand, PHITS overestimates the results for HDPE, Si, SiO_2 and Moon regolith. FLUKA reproduces well the results for HDPE, all the pure and composite lithium-based hydrides and the Moon regolith. Nevertheless, it underestimates the results for the aluminium alloys, Si and SiO_2 . FLUKA tends therefore, to underestimate the results for the heaviest targets. All the Geant4 physics lists used can reproduce well and give consistent results for the aluminium alloys and Si, which are the heaviest tested targets. For all the other cases, QGSP_INCLXX is the list performing the best. QBBC_EMY and FTFP_BERT overestimate the results for HDPE, all the pure and composite lithium-based hydrides, SiO_2 and Moon regolith. These results confirm the recommendation of using QGSP_INCLXX for shielding applications. It should be also noted that QBBC_EMY, which is the reference physics lists recommended for medical and space application, is not able to reproduce well the experimental data for any of the studied materials, but the aluminium alloys.

The differences obtained between different MC codes can be large, reaching 15% for the largest amount of LiH_p . This is due to the different hadronic physics underlying FLUKA,

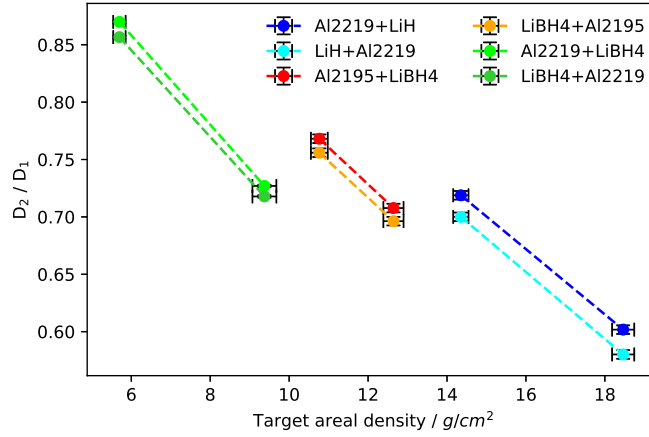


Figure 5: Dose attenuation results obtained merely exchanging the relative order of aluminium (spacecraft structural material) and lithium-based hydrides (shielding material). The dashed lines simply connect the experimental points.

PHITS and different Geant4 physics lists, and in particular, to the different nuclear cross-section parameterisations employed in the codes. These parameterisations are in fact, a crucial ingredient to Monte Carlo simulations (Luoni et al., 2021; Norbury et al., 2020, 2012; Townsend et al., 2002). If a simulation overestimates the dose reduction, the nuclear fragmentation cross-section of the primary ions in the target material is overestimated. The opposite is valid for Monte Carlo simulations underestimating the experimentally measured dose attenuation. Geant4 QBBC.EMY, for instance, underestimates the dose attenuation in HDPE and in all lithium-based hydrides. Therefore, we can deduce that the underlying physics might underestimate the nuclear fragmentation cross-section of 1 GeV/u ^{56}Fe on ^1H target nuclei. Since nuclear cross-section parameterisations are semi-empirical, they need cross-section measurement data to be validated. In Ref. (Luoni et al., 2021) it is shown that no mass-changing cross-sections are present in literature for the systems: $^{56}\text{Fe} + ^{27}\text{Al}$, $^{56}\text{Fe} + ^{28}\text{Si}$ and $^{56}\text{Fe} + ^{16}\text{O}$. This prevents the model validation for such systems and causes more uncertainty in the Monte Carlo simulation results.

A full Bragg curve measurement has been carried out with paraffin. The first part of the curve can be found in Figure 2. The full curve and the Monte Carlo simulation results are reported in Figure 9. In panel (b) of Figure 9, the results obtained with different Geant4 physics lists are reported. Several lists have been used to study the differences in the results introduced by changing the hadronic and electromagnetic models implemented in Geant4. Since QGSP_INCLXX is the list performing the best, the results obtained with it are reported in panel (a) of the same figure, alongside the PHITS and FLUKA results. It can be observed that FLUKA, PHITS and Geant4 QGSP_INCLXX reproduce the fragmentation and tail regions well. PHITS however, underestimates the range of the primaries, and Geant4 QGSP_INCLXX overestimates the height of the Bragg peak. This overestimation is a sign of an underestimation of the nuclear fragmentation processes undergone by the primary Fe ions. In panel (b), it can be observed that the results strongly depend on the reference physics list used. QGSP_BERT.EMV, QBBC.EMY and QGSP_BERT underestimate the Fe nuclear fragmentation processes much stronger than QGSP_INCLXX and FTFP_INCLXX. The latter on the other hand, reproduce well the trend of the data before the Bragg peak and in the tail regions. QGSP_BERT.EMV and QGSP_BERT make use of the Bertini Cascade model at low energies, and QBBC.EMY for some interactions as well. On the other hand, QGSP_INCLXX and FTFP_INCLXX use the Leige Intranuclear Cascade model for proton,

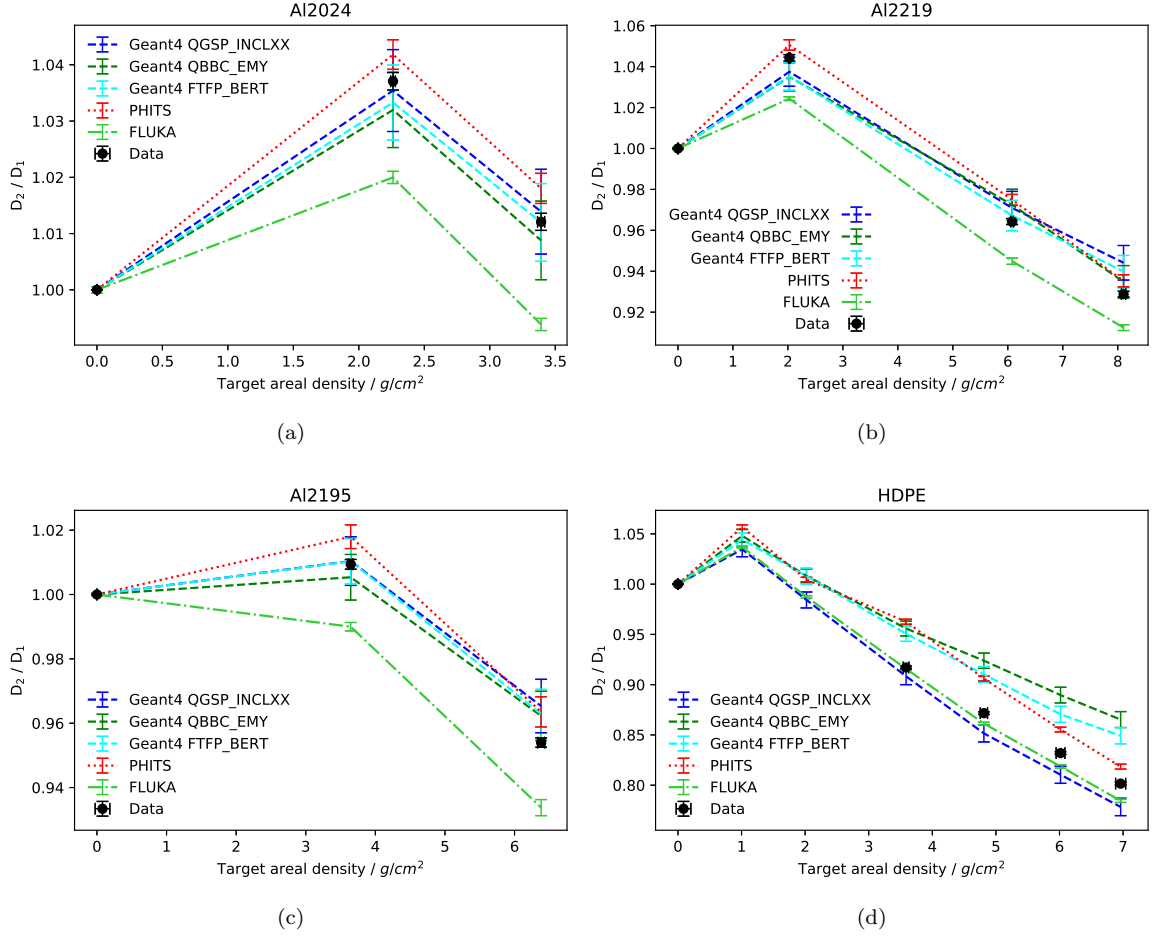


Figure 6: Comparison between experimental data and MC simulation results for the three tested aluminium alloys and for HDPE.

neutron and pion induced reactions at low energies. The differences among the lists look therefore mainly due to low-energy interactions.

4 Conclusions

Absorbed dose attenuation measurements of $1 \text{ GeV/u } ^{56}\text{Fe}$ ions were performed with well-established, innovative and potential *in situ* shielding materials for long-term deep-space exploration. Valuable and precise data were obtained. The addition of paraffin to innovative lithium-based hydrides was proven to be effective to make mechanically and chemically stable promising composite shielding materials. In particular, LiH-paraffin seems to combine the excellent dose attenuation properties of LiH with a manageable chemical stability.

The experimental data were then compared with commonly used MC codes for space exploration simulations, i.e. FLUKA, PHITS, and Geant4. FLUKA resulted to be the best fit with the experimental data for hydrogen-rich materials (HDPE and lithium-based hydrides), while the worst fit for heavier materials such as the aluminium alloys, Si and SiO_2 . In particular, FLUKA overestimates the fragmentation and therefore, the dose attenuation of high-Z materials. For what concerns the paraffin Bragg curve, FLUKA can reproduce well

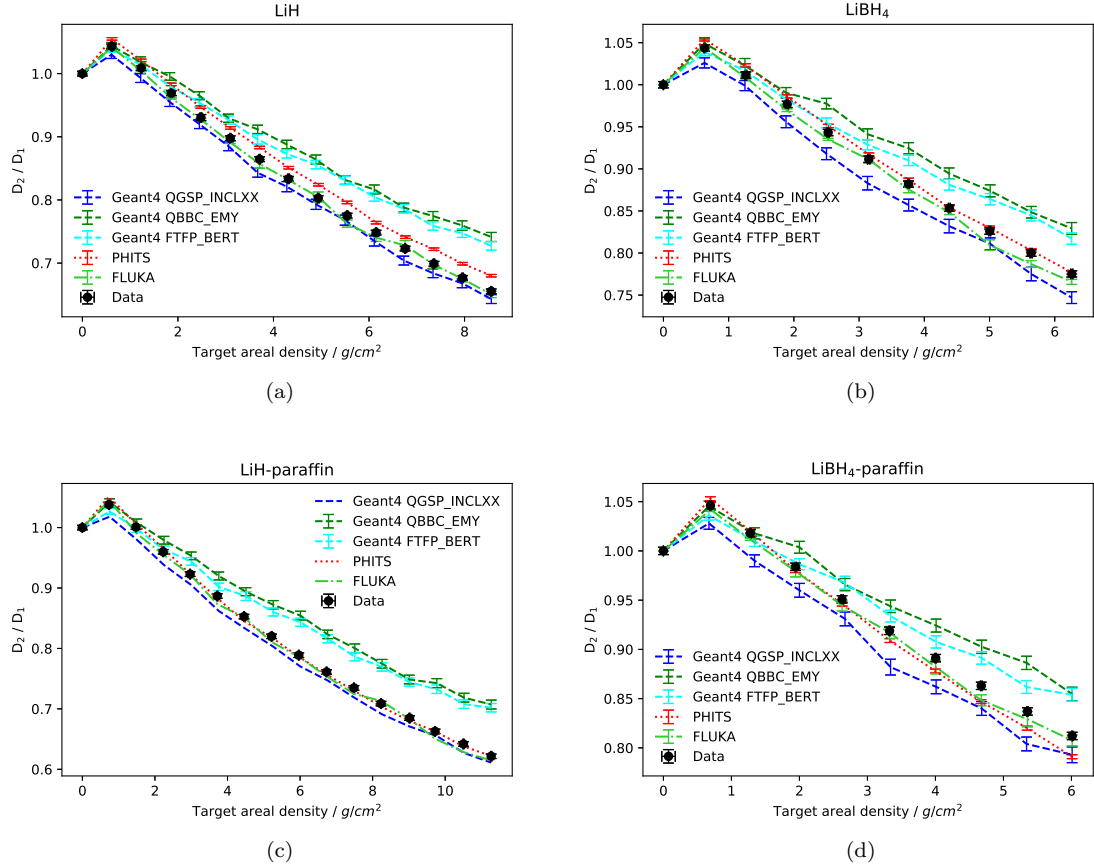


Figure 7: Comparison between experimental data and MC simulation results for the pure and composite lithium-based hydrides.

the first part of it, but it does not match the Bragg peak position and the tail as precisely as Geant4 QGSP_INCLXX does. PHITS fits well the experimentally obtained dose ratios with the lithium-based hydride composites, pure LiBH₄ and paraffin, but tends to underestimate the fragmentation and dose attenuation for all the other tested materials. The Geant4 physics lists results are compatible with each other for heavy targets such as aluminium and Si. These are also the cases in which the Geant4 results fit the data the best. In all the other cases, QGSP_INCLXX is the best fit to the experimental data, while QBBC_EMY and FTFP_BERT underestimate the fragmentation. The more systematic comparison of the Geant4 lists performed for the paraffin Bragg curve, showed a better fit for the lists making use of the Leige Intranuclear Cascade model for low energies (QGSP_INCLXX and FTFP_INCLXX). Overall, the MC simulation results show significant and systematic differences among codes that are used for the same radiation protection purposes. The list performing the best is QGSP_INCLXX, confirming the recommendations of choosing it for shielding applications.

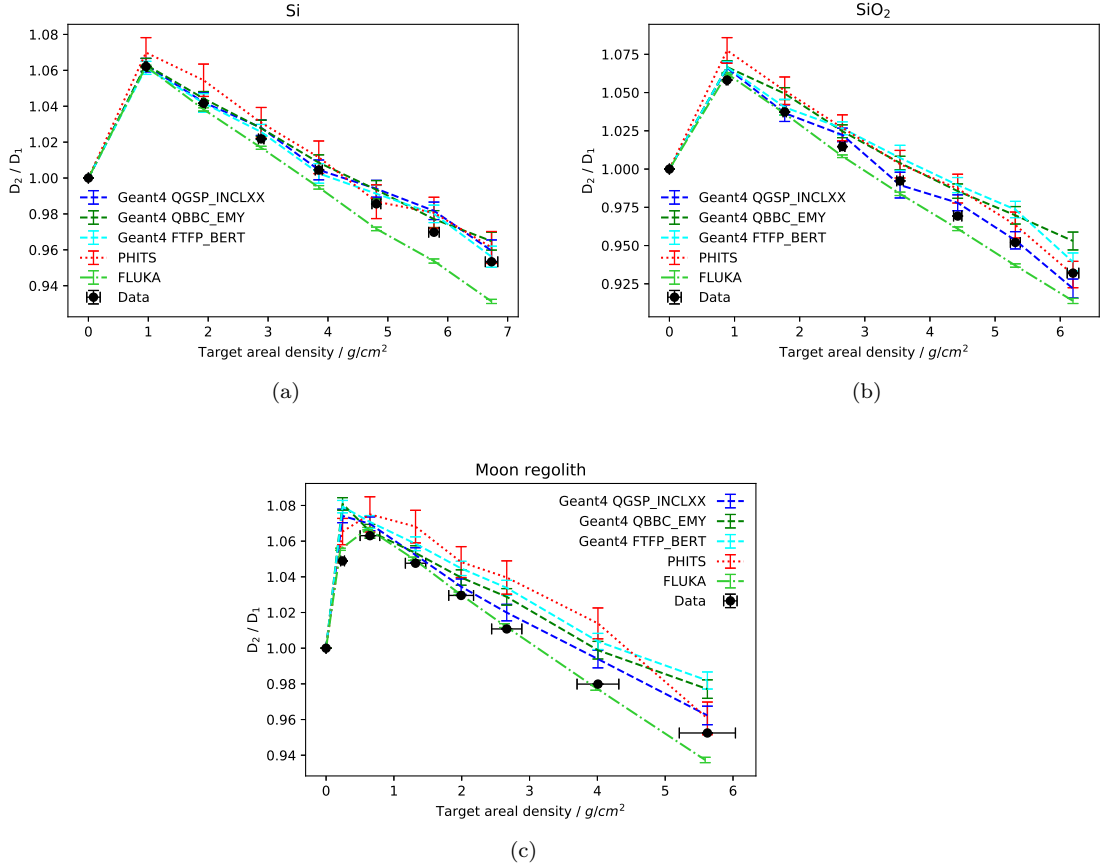


Figure 8: Comparison between experimental data and MC simulation results for Si, SiO₂ and highland Moon regolith.

Appendix A Pure and composite hydrides: production, purity, and homogeneity

The following procedure was selected to obtain compact pellets of pure hydrides. Inside a glove box (MBraun LABstar, working gas Ar 5.5), approximately 20 g of LiH or LiBH₄ were loaded into a mould (65 mm diameter) and a load was applied up to about 12 tons. This load was reached with a stepwise procedure; at each step the load was increased by 3 tons and left for 2 minutes. During holding time, it has been observed that the load of the press decreased because the compaction of the powder was occurring. Finally, the sample was left under the maximum pressure for about 5 minutes. Just after the extraction from the mould, the thickness of the pellet was measured with a caliber and then it was weighted. Finally, the pellet was packaged in a sealed plastic bag, (bi-layered film: PE-nylon) in order to prevent its contact with moisture.

The composites were prepared by directly mixing the hydrides with paraffin in the same glove-box mentioned above. The two systems have been produced using silicon moulds with two different diameter size. For LiH-paraffin samples, a silicon mould (100 mm diameter) was filled with about 30 g of hydride and 30 g of paraffin. The mould and a magnetic stirrer (about 40 mm long) were closed in a PE-nylon bag. The plastic bag was removed from the glove box and the PE bag containing the mould loaded with paraffin+hydrides was inserted in an oven preheated at 85 °C (temperature at which the paraffin is liquid and the plastic

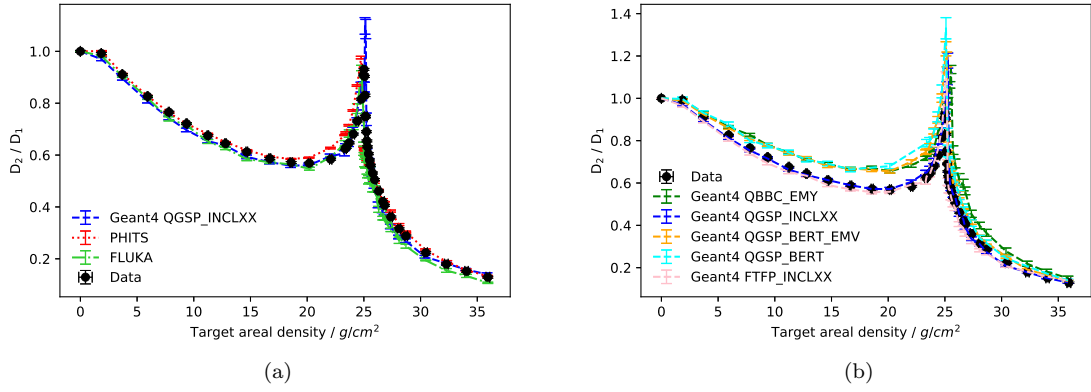


Figure 9: Comparison between experimental data and simulation results for paraffin. In panel (a) simulation results obtained with FLUKA, PHITS and Geant4 physics list QGSP_INCLXX are reported. In panel (b) results obtained with several Geant4 physics lists are shown.

bag still preserves its mechanical and chemical behaviour), holding it for 2 hours at fixed temperature. When the paraffin was completely molten, the magnetic stirrer was inserted in the liquid mixture. The mould was then moved from the oven to a plate pre-heated at 70 °C and stirred for 3 minutes, in order to remove the gas from the liquid. After stirring, the mould was inserted again in the oven and maintained at 85 °C for 20 minutes. This operation has been repeated five times, until bubbles no longer appeared on the surface of the liquid mixture. After cooling down to room temperature, the plastic bag was inserted again inside the glove box, the cooled pellet was removed from the PE/nylon bag and the solid pellet was extracted from the mould. The exceeding composite was removed by abrading the surface with a sandpaper and the pellet was enveloped in a PE bag and closed under vacuum for storage. The same method has been applied for preparing LiBH₄-paraffin composites, mixing the two components with a 12g:8g ratio in a silicon mould of 60 mm diameter.

The crystalline phases present in the prepared samples have been determined by X-ray diffraction using a MalvernPanalytical Xpert PRO MPD diffractometer with Cu anode and Bragg-Brentano geometry. The results are reported in Figure A1. It is clear that the preparation of samples does not introduce any contamination or microstructural changes.

The homogeneity of the filler distribution in the paraffin matrix was determined by an Oxford INCA Energy-dispersive X-ray spectroscopy coupled with a Scanning Electron Microscope Zeiss EVO 50. By carrying out Energy dispersive X-ray spectroscopy mappings, and taking into account the instrumental limits of the elemental detection of such technique (detection of elements with $Z \geq 6$), the distribution of the hydride in the paraffin matrix has been indirectly verified looking at the oxygen distribution. Pure hydrides are very sensitive to the moisture, and they quickly degrade towards reaction products, forming hydroxide or hydrated species of the hydrides. As an example, in Figure A2, the oxygen mapping in LiH-paraffin sample (50% w/w) is shown. The red colour is uniformly distributed over the samples, confirming that the hydride is homogeneously dispersed in the composite. The homogeneity of the dispersion of the hydrides was also studied in the vertical section of the sample. To have an objective demonstration that there is no sedimentation of the charge due to gravity during solidification both parallel flat surfaces have been subjected to XRD. If there was no sedimentation the diffractograms should be comparable and the intensity of

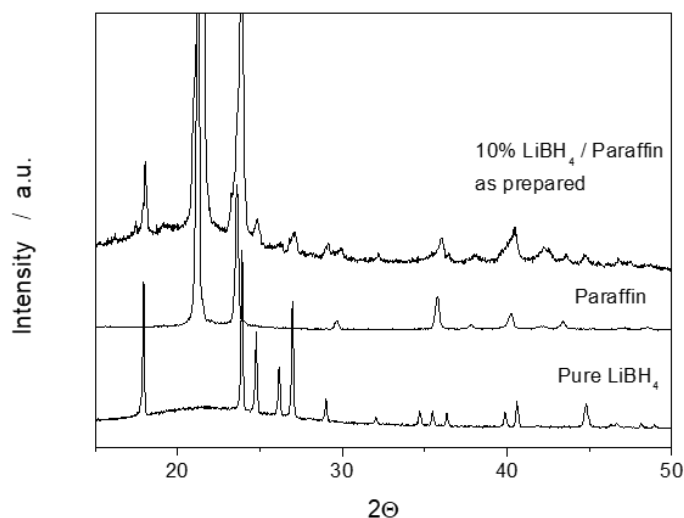


Figure A1: XRD patterns of LiBH_4 , paraffin and composite $\text{LiBH}_4(10\%)\text{-paraffin}$

the reflexes due to the charge should be about the same. The patterns collected on the two different faces (not shown) were comparable, confirming no sedimentation by the filler, i.e. a homogeneous dispersion of it.

Appendix B Longevity of LiH and LiBH_4 -paraffin composites

In Figure B1, are reported XRD patterns (B D, 1978) collected with 10% wt. of LiH (panel (a)) and 10 wt.% of LiBH_4 (panel (b)) in paraffin at different times after preparation. In panel (a), immediately after preparation (t_0), diffraction peaks of LiH and paraffin can be observed. Additionally, a rather small signal due to the LiOH phase can be seen around a diffraction angle of 33° , suggesting that the charge (LiH) undergoes a small hydration reaction during the synthesis of the composite. With increasing time of exposure to air, XRD signals related to the degradation products increase in intensity. Firstly, lithium hydroxide is generated and, subsequently, its hydrate form ($\text{LiOH}\cdot\text{H}_2\text{O}$) starts to appear. These results suggest that the kinetics of lithium hydride degradation with moisture within the composite is rather low, as the charge signals are still present even after 2 weeks of exposure of the sample to air. The main degradation products observed when the composite is exposed to air are LiOH and $\text{LiOH}\cdot\text{H}_2\text{O}$, suggesting that the paraffin presence hinders the formation of Li_2CO_3 , observed as degradation product of pristine LiH (Machin & Tompkins, 1966). In conclusion, the addition of paraffin acts as an effective protective barrier for the hydride phase, so that the degradation kinetics is greatly reduced. It is worth noting that, after 2 weeks of exposure, LiH remains as the main filler phase in the composite, as shown by the presence of corresponding XRD peaks in panel (a) of Figure B1.

In panel (b), it can be observed that as soon as the LiBH_4 -paraffin composite was taken out of the glove box, it did not show evidence of degradation. This means that during the synthesis, the hydride has not undergone decomposition reactions. After 16 hours of exposure, however, in addition to the LiBH_4 XRD peaks, which are still present, the composite begins to show new signals due to the appearance of compounds formed by hydration of the hydride. In particular, the XRD peaks of degradation $\text{LiB}(\text{OH})_4$ compound

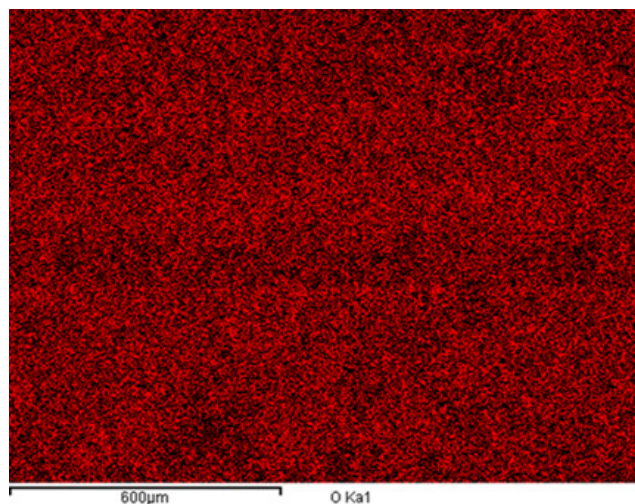
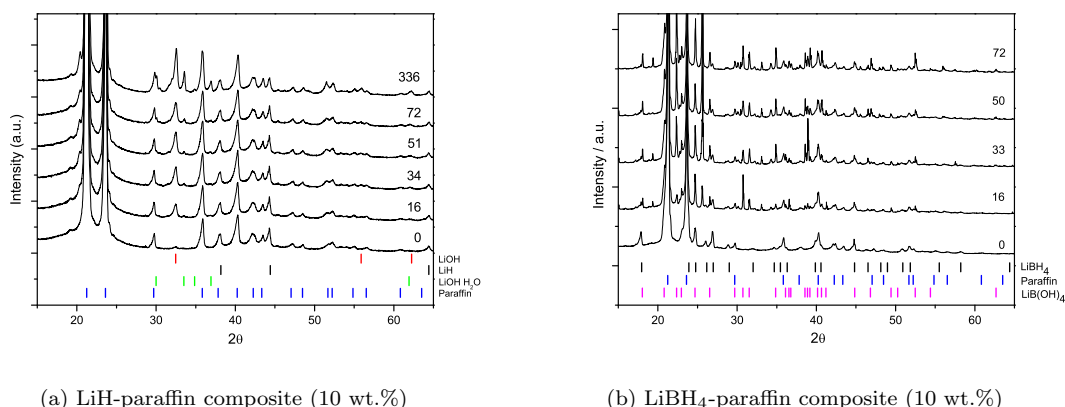


Figure A2: EDS mapping on LiH-Paraffin sample (50% w/w)



(a) LiH-paraffin composite (10 wt.%)

(b) LiBH₄-paraffin composite (10 wt.%)

Figure B1: XRD patterns of LiH and LiBH₄-paraffin composite (10 wt.%) collected at different times (in hours) after preparation. Vertical bars correspond to diffraction peak position for crystal phases reported on the right side.

increase in intensity over time, at the expense of the charge-related signals, which decrease until they finally disappear after around 72 hours. Also in this case the presence of paraffin greatly reduces the degradation kinetics of the hydride. In fact, such a degradation due to the reaction with the moisture to form LiB(OH)₄ is practically instantaneous for pure LiBH₄, while it needs approximately 3 days for the composite, as shown by the absence of XRD peaks related to LiBH₄ in panel (b) of Figure B1.

Appendix C Post irradiation test characterisation

As reported in Appendix A, pure hydrides and composites pellets were protected by a by-layered Nylon/PE bag. X-ray diffraction analysis was performed on composite pellets after the irradiation experimental campaigns with the aim of checking the chemical degradation

of the samples caused by potential packaging defects or failure, or by the irradiation itself (radiolysis). Results are reported in Figure C1, for LiH (pattern a) and LiBH₄ (pattern b), together with an XRD pattern of the Nylon/PE bag (pattern c). In Figure C1 (pattern a),

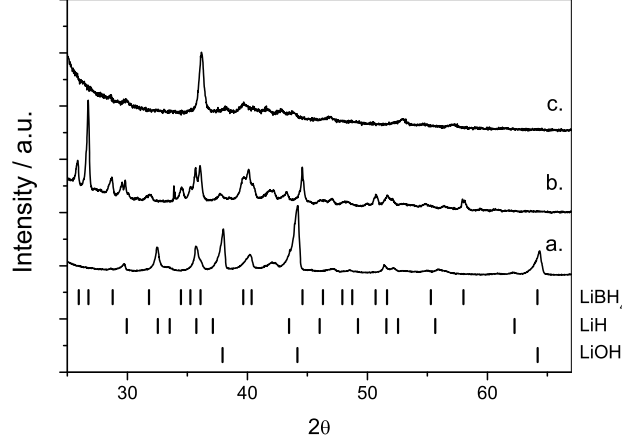


Figure C1: XRD patterns after irradiation experiments of LiH-paraffin composite (50 wt.%) (pattern a) and LiBH₄-paraffin composite (40 wt.%) (pattern b) embedded in Nylon/PE bag. The pattern of the Nylon/PE bag is also reported for comparison (pattern c).

together with XRD peaks related to the paraffin matrix and the Nylon/PE bag, those due to the LiH phase can be observed. In addition, a weak XRD peak due to the LiOH phase is also present at about 33° 2θ, suggesting that the occurrence of a reaction with moisture still occurred. As suggested by the longevity test of section Appendix B, Figure C1 (pattern b) confirms that LiBH₄ composite pellets has a strong stability against hydration processes, since no extra diffraction peaks appear in the pattern.

Appendix D Dose build-up

A small dose build-up can be seen for the very first g cm⁻² of material. It should be noted that it is not observed for paraffin since the thinnest target irradiated is already much thicker than the maximum build-up depth. It is due to additional particles generated within the target material, which are mainly forward directed. The depth of the dose build-up effect corresponds to the range of such particles in the target material. After the build-up effect reaches equilibrium at a certain depth, the dose attenuation due to projectile fragmentation takes over and the dose ratio starts to decrease. This effect is much stronger for lighter ions (Giraud et al., 2018). Additional MC simulations have been performed with FLUKA to deepen the phenomenon. The results obtained for LiH and Al₂₂19 are reported in Figure D1. They show that the build-up observed in the experimental data is merely due to delta electrons. The target fragments generated through nuclear interactions between the ⁵⁶Fe ions and the target nuclei do not contribute to it. This is very different than what happens with light-ion beams. The curve in magenta reports the simulation results obtained when no delta electrons are generated. The electronic production threshold was set to 57 GeV, which is higher than the kinetic energy of the primary ions. On the other hand, the light green curve was generated through setting the electronic production threshold to 0.1 MeV. Some additional points are reported with respect to panel (a) of Figure 7 with the

510 aim of showing the actual depth of the build-up effect, which is smaller than the first LiH thickness used.

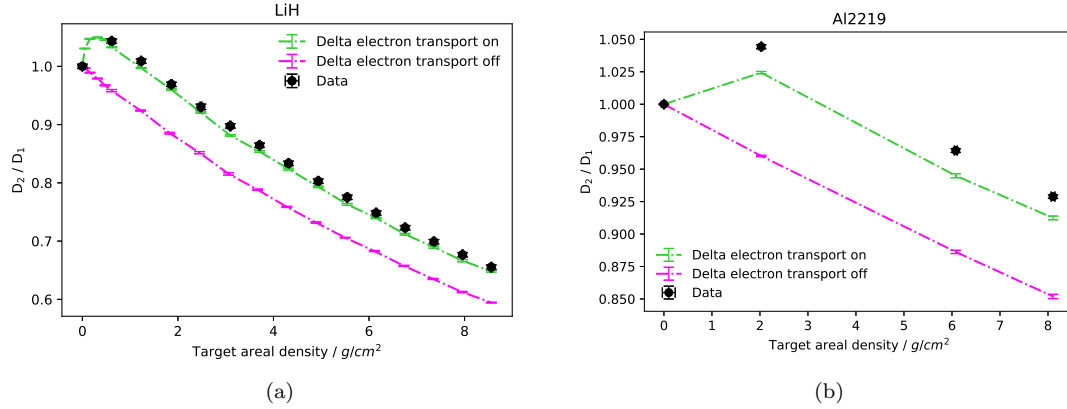


Figure D1: Comparison between the result of MC simulations performed with FLUKA for pure-LiH target (panel (a)) and Al2219 (panel (b)), including (light green) and excluding (magenta) the dose contribution of delta electrons.

511

512 Appendix E Multi-layer configurations

513 Some realistic multi-layer configurations have been used for dose attenuation measurements.
 514 Similar measurements were already performed in the past ROSSINI2 campaign (Giraud et
 515 al., 2018). The materials used for these tests are: one of the aluminium alloys described in
 516 Section 2.1, LiBH₄ and simulants of Moon regolith and concrete. The Moon regolith used
 517 for the multi-layer measurements is not the same as for the single material irradiations. It
 518 is JSC-1 Moon regolith in dust form (not pressed) and enclosed inside three T75 Falcon
 519 Tissue Culture Treated Flasks. The Moon concrete is produced by mixing this regolith
 520 with a chemical binder. More details about the Moon regolith and concrete used for the
 521 multi-layer configurations can be found in reference (Giraud et al., 2018). The results
 522 are reported in Figure E1 alongside simulation results obtained with PHITS and Geant4
 523 (QGSP_INCLXX physics list). ML1 stays for “Multi-Layer 1” and it is made of Moon
 524 regolith + Al2219 + LiBH₄. ML2 is made of Moon concrete + Al2219 + LiBH₄, and ML3
 525 of Al2195 + LiBH₄. ML1 and ML2 are supposed to reproduce realistic *in situ* material
 526 configurations, one of which made out of pure Moon regolith and another of Moon concrete.
 527 ML3 on the other hand, reproduces a spacecraft material configuration. The lower the ratio
 528 is, the better the configuration for shielding from 1 GeV/u ⁵⁶Fe is. The agreement between
 529 experimental data and simulation results is generally good, even if the simulations tend
 530 to underestimate the experimental results. A disagreement of about 10% is found for ML1
 531 (28.4 g cm⁻²). The total areal density of such configuration is 28.4 g cm⁻². This thickness
 532 lays close to the Bragg peak region, where by definition, the absorbed dose varies greatly
 533 with the target thickness. Therefore, even small thickness uncertainties can result in a large
 534 error in the simulated dose.

535 Funding

536 This work was supported by the European Space Agency with the ROSSINI3 project [Con-
 537 tract No. 4000125785/ 18/NL/GLC], which was led by Thales Alenia Space Italia. The

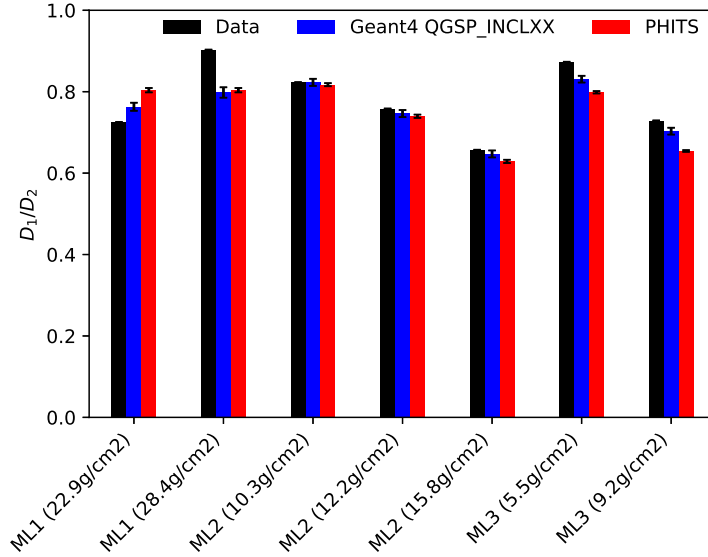


Figure E1: Experimental and simulation results for multi-layer configurations. In abscissa, the multi-layer acronyms are reported, alongside their areal densities. ML1 stays for “Multi-Layer 1” and it is made of Moon regolith + Al2219 + LiBH₄. ML2 is made of Moon concrete + Al2219 + LiBH₄, and ML3 of Al2195 + LiBH₄. For the same configurations with different areal densities, only the LiBH₄ content is different.

measurements were performed in GSI Helmholtzzentrum für Schwerionenforschung in Darmstadt (Germany) Cave A, in the frame of FAIR Phase-0.

Contributions

FL, UW, DB, FH, CAR, CS and LB performed the experiments. UW and FL wrote the parts of the manuscript related to the experimental work. GF, AB and MB made the samples and wrote the parts related to them. FL performed the FLUKA simulations and wrote about them. LB performed the Geant4 simulations and wrote about them. MG and CC performed the PHITS simulations and wrote about them. FL coordinated the manuscript writing. UW, MB, MG, GS and MD coordinated the work. In particular, UW coordinated the experimental work, MB the sample generation work, GS and MG the ROSSINI3 project, together with the help of MD. All authors contributed to the manuscript writing.

References

- Agostinelli, S., Allison, J., Amako, K., Apostolakis, J., Araujo, H., Arce, P., ... Zschiesche, D. (2003). Geant4—a simulation toolkit. *Nucl. Instrum. Methods Phys. Res. A*, 506(3), 250-303. Retrieved from <https://www.sciencedirect.com/science/article/pii/S0168900203013688> doi: [https://doi.org/10.1016/S0168-9002\(03\)01368-8](https://doi.org/10.1016/S0168-9002(03)01368-8)
- Aricò, G., Ferrari, A., Horst, F., Mairani, A., Reidel, C., Schuy, C., & Weber, U. (2019). Developments of the nuclear reaction and fragmentation models in FLUKA for ion collisions at therapeutic energies. *CERN Proc.*, 1, 321–326.
- B D, C. (1978). *Elements of x-ray diffraction* (Addison-Wesley, Ed.). Addison-Wesley publishing company, inc.

- Borak, T. B., Heilbronn, L. H., Townsend, L. W., McBeth, R. A., & de Wet, W. (2014). Quality factors for space radiation: A new approach. *Life Sci. Space Res.*, 1, 96-102. Retrieved from <https://www.sciencedirect.com/science/article/pii/S221455241400011X> doi: <https://doi.org/10.1016/j.lssr.2014.02.005>
- Boscolo, D., Scognamiglio, D., Horst, F., Weber, U., Schuy, C., Durante, M., ... Zbořil, M. (2020). Characterization of the secondary neutron field produced in a thick aluminum shield by 1 gev/u 56fe ions using tld-based ambient dosimeters. *Front. Phys.*, 8, 365. Retrieved from <https://www.frontiersin.org/article/10.3389/fphy.2020.00365> doi: 10.3389/fphy.2020.00365
- Böhlen, T., Cerutti, F., Chin, M., Fassò, A., Ferrari, A., Ortega, P., ... Vlachoudis, V. (2014). The fluka code: Developments and challenges for high energy and medical applications. *Nucl. Data Sheets*, 120, 211-214. Retrieved from <https://www.sciencedirect.com/science/article/pii/S0090375214005018> doi: <https://doi.org/10.1016/j.nds.2014.07.049>
- Carlsson, C., & Carlsson, G. (1977). Proton dosimetry with 185 mev protons. *Health Phys.*, 33(5), 481-484.
- Castellanos, L., McGirl, N., Srikrishna, A., Heilbronn, L., La Tessa, C., Rusek, A., ... Zeitlin, C. (2017). Thick-target yields of secondary ions and neutrons for validation of radiation transport codes. In *2017 ieee aerospace conference* (p. 1-10). doi: 10.1109/AERO.2017.7943575
- Chancellor, J., Scott, G., & Sutton, J. (2014). Space Radiation: The Number One Risk to Astronaut Health beyond Low Earth Orbit. *Life*.
- Council, N. R., et al. (2008). *Managing space radiation risk in the new era of space exploration*. National Academies Press.
- Cucinotta, F., Kim, M.-H., Chappell, L., & Huff, J. (2013). How safe is safe enough? radiation risk for a human mission to mars. *PloS one*, 8(10), e74988. doi: <https://doi.org/10.1371/journal.pone.0074988>
- Durante, M. (2008). Physical and biomedical countermeasures for space radiation risk. *Z. Med. Phys.*, 18(4), 244-252. Retrieved from <https://www.sciencedirect.com/science/article/pii/S0939388908000846> doi: <https://doi.org/10.1016/j.zemedi.2008.06.010>
- Durante, M., & Cucinotta, F. (2011, Nov). Physical basis of radiation protection in space travel. *Rev. Mod. Phys.*, 83, 1245-1281. Retrieved from <https://link.aps.org/doi/10.1103/RevModPhys.83.1245> doi: 10.1103/RevModPhys.83.1245
- Ferrari, A., Sala, P., Fassò, A., Ranft, J., Siegen, U., et al. (2005). Fluka: a multi-particle transport code [Computer software manual].
- Geant4 physics reference manual, release 10.6 [Computer software manual]. (2017). Retrieved from <http://geant4-userdoc.web.cern.ch/geant4-userdoc/UsersGuides/PhysicsReferenceManual/fo/PhysicsReferenceManual.pdf>
- Giraud, M., Schuy, C., Weber, U., Rovituso, M., Santin, G., Norbury, J., ... La Tessa, C. (2018, 08). Accelerator-Based Tests of Shielding Effectiveness of Different Materials and Multilayers using High-Energy Light and Heavy Ions. *Radiation Research*, 190(5), 526-537. Retrieved from <https://doi.org/10.1667/RR15111.1> doi: 10.1667/RR15111.1
- Guetersloh, S., Zeitlin, C., Heilbronn, L., Miller, J., Komiyama, T., Fukumura, A., ... Bhattacharya, M. (2006). Polyethylene as a radiation shielding standard in simulated cosmic-ray environments. *Nucl. Instrum. Methods Phys. Res. B*, 252(2), 319-332. Retrieved from <https://www.sciencedirect.com/science/article/pii/S0168583X06008822> doi: <https://doi.org/10.1016/j.nimb.2006.08.019>
- Horst, F., Boscolo, D., Durante, M., Luoni, F., Schuy, C., & Weber, U. (2022). Thick shielding against galactic cosmic radiation: a monte carlo study with focus on the role of secondary neutrons. *submitted to Life Sci. Space Res.*
- Ivantchenko, A. V., Ivanchenko, V. N., Molina, J.-M. Q., & Incerti, S. L. (2012). Geant4 hadronic physics for space radiation environment. *Int. J. Radiat. Biol.*, 88(1-2), 171-175. Retrieved from <https://doi.org/10.3109/09553002.2011.610865> doi: 10

- .3109/09553002.2011.610865
- Iwase, H., Niita, K., & Nakamura, T. (2002). Development of general-purpose particle and heavy ion transport monte carlo code. *Journal of Nuclear Science and Technology*, 39(11), 1142-1151. Retrieved from <https://doi.org/10.1080/18811248.2002.9715305> doi: 10.1080/18811248.2002.9715305
- Kennedy, A. (2014). Biological effects of space radiation and development of effective countermeasures. *Life Sci. Space Res.*, 1, 10-43. Retrieved from <https://www.sciencedirect.com/science/article/pii/S2214552414000108> doi: <https://doi.org/10.1016/j.lssr.2014.02.004>
- La Tessa, C., Guetersloh, S., Heilbronn, L., Miller, J., Sihver, L., & Zeitlin, C. (2005). Fragmentation of 1gev/nucleon iron ions in thick targets relevant for space exploration. *Adv. Space Res.*, 35(2), 223-229. Retrieved from <https://www.sciencedirect.com/science/article/pii/S0273117705001730> (Space Life Sciences: Ground-Based Iron-Ion Biology and Physics, Including Shielding) doi: <https://doi.org/10.1016/j.asr.2005.02.007>
- Lobascio, C., Briccarello, M., Destefanis, R., Faraud, M., Gialanella, G., Grossi, G., ... Durante, M. (2008). Accelerator-based tests of radiation shielding properties of materials used in human space infrastructures. *Health Phys.*, 94(3). doi: 10.1097/01.HP.0000288560.21906.4e
- Luoni, F., Horst, F., Reidel, C., Quarz, A., Bagnale, L., Sihver, L., ... Durante, M. (2021). Total nuclear reaction cross-section database for radiation protection in space and heavy-ion therapy applications. *New J. Phys.*, 23(101201). doi: <https://doi.org/10.1088/1367-2630/ac27e1>
- Machin, W. D., & Tompkins, F. C. (1966). Kinetics of the reaction of water vapour with crystalline lithium hydride. *J. Chem. Soc., Faraday trans.*, 62, 2205—2218.
- Miller, J., Zeitlin, C., Cucinotta, F., Heilbronn, L., Stephens, D., & Wilson, J. (2003). Benchmark studies of the effectiveness of structural and internal materials as radiation shielding for the international space station. *Radiat. Res.*, 159(3), 381-390. doi: 10.1667/0033-7587(2003)159[0381:BSOTEO]2.0.CO;2
- Naito, M., Kodaira, S., Ogawara, R., Tobita, K., Someya, Y., Kusumoto, T., ... ichi Orimo, S. (2020). Investigation of shielding material properties for effective space radiation protection. *Life Sci. Space Res.*, 26, 69-76. Retrieved from <https://www.sciencedirect.com/science/article/pii/S2214552420300377> doi: <https://doi.org/10.1016/j.lssr.2020.05.001>
- Norbury, J., Battistoni, G., Besuglow, J., Bocchini, L., Boscolo, D., Botvina, A., ... Zeitlin, C. (2020). Are Further Cross Section Measurements Necessary for Space Radiation Protection or Ion Therapy Applications? Helium Projectiles. *Front. Phys.*, 8, 409.
- Norbury, J., Miller, J., Adamczyk, A., Heilbronn, L., Townsend, L., Blattnig, S., ... Zeitlin, C. (2012). Nuclear data for space radiation. *Radiat. Meas.*, 47(5), 315 - 363. Retrieved from <http://www.sciencedirect.com/science/article/pii/S1350448712000686> doi: <https://doi.org/10.1016/j.radmeas.2012.03.004>
- Pfuhl, T., Horst, F., Schuy, C., & Weber, U. (2018, aug). Dose build-up effects induced by delta electrons and target fragments in proton bragg curves—measurements and simulations. *Phys. Med. Biol.*, 63(17), 175002. Retrieved from <https://doi.org/10.1088/1361-6560/aad8fc> doi: 10.1088/1361-6560/aad8fc
- Schuy, C., La Tessa, C., Horst, F., Rovituso, M., Durante, M., Giraudo, M., ... Weber, U. (2018, 11). Experimental Assessment of Lithium Hydride's Space Radiation Shielding Performance and Monte Carlo Benchmarking. *Radiat. Res.*, 191(2), 154-161. Retrieved from <https://doi.org/10.1667/RR15123.1> doi: 10.1667/RR15123.1
- Shavers, M., Zapp, N., Barber, R., Wilson, J., Qualls, G., Toupes, L., ... Cucinotta, F. (2004). Implementation of alara radiation protection on the iss through polyethylene shielding augmentation of the service module crew quarters. *Adv. Space Res.*, 34(6), 1333-1337. doi: <https://doi.org/10.1016/j.asr.2003.10.051>
- Simeonov, Y., Weber, U., Penchev, P., Ringbæk, T. P., Schuy, C., Brons, S., ... Zink, K. (2017, aug). 3d range-modulator for scanned particle therapy: development,

- monte carlo simulations and experimental evaluation. *Phys. Med. Biol.*, 62(17), 7075–7096. Retrieved from <https://doi.org/10.1088/1361-6560/aa81f4> doi: 10.1088/1361-6560/aa81f4
- Simpson, J. (1983). Elemental and isotopic composition of the galactic cosmic rays. *Annual Review of Nuclear and Particle Science*, 33(1), 323-382.
- Townsend, L., Cucinotta, F., & Heilbronn, L. (2002). Nuclear model calculations and their role in space radiation research. *Adv. Space Res.*, 30(4), 907-916. Retrieved from <https://www.sciencedirect.com/science/article/pii/S0273117702004052> doi: [https://doi.org/10.1016/S0273-1177\(02\)00405-2](https://doi.org/10.1016/S0273-1177(02)00405-2)
- Vlachoudis, V., et al. (2009). Flair: a powerful but user friendly graphical interface for fluka. In *Proc. int. conf. on mathematics, computational methods & reactor physics (m&c 2009), saratoga springs, new york* (Vol. 176).
- Washburn, S., Blattnig, S., Singleterry, R., & Westover, S. (2015). Active magnetic radiation shielding system analysis and key technologies. *Life Sci. Space Res.*, 4, 22-34. Retrieved from <https://www.sciencedirect.com/science/article/pii/S2214552414000686> doi: <https://doi.org/10.1016/j.lssr.2014.12.004>
- Zeitlin, C., Guetersloh, S., Heilbronn, L., & Miller, J. (2006). Measurements of materials shielding properties with 1gev/nuc 56fe. *Nucl. Instrum. Methods Phys. Res. B*, 252(2), 308-318. Retrieved from <https://www.sciencedirect.com/science/article/pii/S0168583X06008809> doi: <https://doi.org/10.1016/j.nimb.2006.08.011>
- Zeitlin, C., Guetersloh, S., Heilbronn, L., Miller, J., Elkhayari, N., Empl, A., ... Kuznetsov, E. (2008, jul). Shielding experiments with high-energy heavy ions for spaceflight applications. *New J. Phys.*, 10(7), 075007. Retrieved from <https://doi.org/10.1088/1367-2630/10/7/075007> doi: 10.1088/1367-2630/10/7/075007
- Zeitlin, C., & La Tessa, C. (2016). The role of nuclear fragmentation in particle therapy and space radiation protection. *Front. Oncol.*, 6, 65. Retrieved from <https://www.frontiersin.org/article/10.3389/fonc.2016.00065> doi: 10.3389/fonc.2016.00065